

High-Reynolds-number turbulence in small apparatus: grid turbulence in cryogenic liquids

By CHRISTOPHER M. WHITE[†], ADONIOS N. KARPETIS[‡] AND KATEPALLI R. SREENIVASAN

Mason Laboratory, Yale University, New Haven, CT 06520-8286, USA

(Received 17 June 2001 and in revised form 18 October 2001)

Liquid helium at 4.2 K has a viscosity that is about 40 times smaller than that of water at room temperature, and about 600 times smaller than that of air at atmospheric pressure. It is therefore a convenient fluid for generating in a table-top apparatus turbulent flows at high Reynolds numbers that require large air and water facilities. Here, we produce turbulence behind towed grids in a liquid helium chamber that is 5 cm² in cross-section at mesh Reynolds numbers of up to 7×10^5 . Liquid nitrogen is intermediate in its viscosity as well as refrigeration demands, and so we also exploit its use to generate towed-grid turbulence up to mesh Reynolds number of about 2×10^4 . In both instances, we map two-dimensional fields of velocity vectors using particle image velocimetry, and compare the data with those in water and air.

1. Introduction

Fluid turbulence is essentially a high-Reynolds-number phenomenon. There has therefore been a push towards attaining increasingly higher Reynolds numbers, especially for determining the applicable scaling laws. High Reynolds numbers can be generated by using either large flow facilities or fluids of small viscosity. Cryogenic helium has the smallest viscosity of any known substance; for example, in the liquid state at 4.2 K, its kinematic viscosity $\nu \approx 2.5 \times 10^{-4} \text{ cm}^2 \text{ s}^{-1}$. While the attractions of this low viscosity have been appreciated amply (see Donnelly & Sreenivasan 1998 for a summary), cryogenic technology has not yet caught on in isothermal turbulence studies. One reason is the difficulty in making velocity measurements with adequate resolution: the smallness of the apparatus, which is otherwise of great benefit, implies smaller turbulent scales for a given Reynolds number. For the helium technology to become competitive, one has to show, in particular, that the standard turbulence measurements that are now possible in water and air are equally feasible in helium. While there already exist single-point measurements of temperature and velocity in helium turbulence (e.g. Wu 1991; Castaing, Chabaud & Hebral 1992; Tabeling *et al.* 1996; Stalp, Niemela & Donnelly 2000), no attempts have yet been made to obtain planar maps of the velocity field using particle image velocimetry (PIV). Making such measurements is our goal here.

First, we use liquid helium to generate in a table-top apparatus, whose working section is 5 cm square, well-behaved turbulence behind towed grids at mesh Reynolds numbers of up to 7×10^5 . For comparison, the towed-grid water measurements of Dickey & Mellor (1980) were made in a tank of cross-sectional area about 174

[†] Present address: Department of Mechanical Engineering, Stanford University, CA 94305, USA.

[‡] Present address: Sandia National Laboratory, MS 9051, Livermore, CA 94511, USA.

times larger, yet the mesh Reynolds number was about 15 times smaller than the largest attained here. Second, we make velocity measurements in plane sections of this flow using PIV, and demonstrate that detailed characterization of high-Reynolds-number turbulence in a table-top apparatus is eminently feasible. (The limitations that still exist are not intrinsic.) Third, while cryogenic helium offers the best means for attaining the highest possible Reynolds numbers, it is also demanding in terms of refrigeration. A fluid intermediate in its viscosity as well as refrigeration needs is liquid nitrogen. It is an easier fluid for PIV measurements because finding suitable tracer particles is relatively easy. Using the same apparatus as before, we perform identical measurements in liquid nitrogen and compare the results to those in liquid helium. The highest mesh Reynolds number is of the order of 2×10^4 , about half Dickey & Mellor's.

We chose grid turbulence for two reasons, quite aside from the intrinsic interest in the flow. First, nearly homogeneous and isotropic turbulence behind grids has been studied extensively (e.g. Batchelor & Townsend 1948; Comte-Bellot & Corrsin 1966; Gad-el-Hak & Corrsin 1974; Sreenivasan *et al.* 1980; Mohamed & LaRue 1990), and its analogue has been simulated numerically in a periodic box (e.g. Chen *et al.* 1993; Jimenez *et al.* 1993; Vincent & Meneguzzi 1994). It is thus possible to make accurate checks on the present results. Second, if the PIV technique can be made to work in the grid experiment, for which the mean velocity is zero and fluctuations in all three directions are comparable, its success is likely to be assured in most other helium flows as well.

2. Experimental details

Only a brief description is presented here. More details are given in White (2001).

2.1. The cryostat

A cut-away drawing of the apparatus is shown in figure 1. Its footprint is about 30 cm^2 . The inner chamber, 5 cm^2 in cross-section and 25 cm in height, contains liquid helium. A port at the top of the inner chamber connects it to a helium bath above, and prevents the formation of a free surface. Surrounding the inner chamber is a radiation shield maintained at liquid nitrogen temperature (77 K), which itself is isolated from an external chamber at ambient temperature. The spaces between the chambers are evacuated to $\approx 1 \mu\text{Torr}$ to diminish heat loss. Each chamber is fitted for optical access with a set of four aligned windows centred at the midpoint of the inner chamber.

Turbulence is generated by pulling a biplane square grid of solidity 0.44 through the stagnant column of liquid helium at 4.2 K. Three grids with mesh sizes of 2.5, 3.33 and 7.15 mm are used. The grids are towed with a linear servo actuator capable of accelerations up to 15g and velocities up to 8 m s^{-1} . Grid speeds of $50\text{--}200 \text{ cm s}^{-1}$ are generated using start-up accelerations of $10\text{--}50 \text{ m s}^{-2}$. The towing speeds are constant over a sizeable part of the traverse – for example, over 80% of the channel height for the acceleration of 20 m s^{-2} .

2.2. Tracer particles

A challenging aspect of PIV measurements in liquid helium is that its low dynamic viscosity and density encourage most particles to settle rather rapidly. For instance, a $1 \mu\text{m}$ solid glass particle settles five times faster in liquid helium than in air at room temperature. This tendency and the smallness of scales demand the use of the smallest particles possible, but the particles cannot be too small because the scattered light then

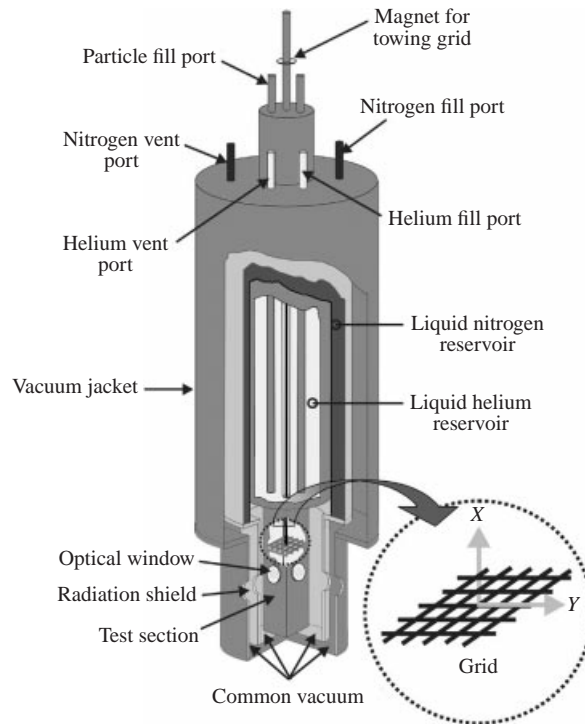


FIGURE 1. Cut-away schematic of the experimental apparatus.

becomes too weak. After considerable study (White 2001), we have chosen hollow glass spheres. The current technology can produce sizes of the order of $1\ \mu\text{m}$. The nominal density of these particles is about $0.13\ \text{g cm}^{-3}$, which compares favourably to that of liquid helium of $0.125\ \text{g cm}^{-3}$ at 4.2 K.

In reality, the control in making hollow glass spheres is poor, and so their diameters range from 1 to $10\ \mu\text{m}$ and their densities from 0.13 to $0.5\ \text{g cm}^{-3}$. In our measurements, the heavier spheres settle to the bottom of the tank quickly and the smaller ones, comparable to the smallest turbulent length scales generated in the flow, stay effectively suspended. These are the particles used for PIV. Their estimated settling velocities confirm that the Stokes and Froude numbers are less than 0.07 during the measurement period, so it is reasonable to assume that they track the fluid motion adequately (see, for example, Maxey & Riley 1983; Mei, Adrian & Hanratty 1991).

The particle selection for liquid nitrogen is almost trivial by comparison. We use solid latex spheres $3.2\ \mu\text{m}$ in diameter. Their Stokes and Froude numbers are an order of magnitude smaller than those of the tracer particles used in liquid helium.

2.3. Particle image velocimetry

The particles are illuminated for 10 ns by light sheets from a red laser (wavelength 640 nm) and a green laser (532 nm) superimposed in space but separated in time by a well-regulated amount (of the order of a few ms). The light sheet thickness is approximately $500\ \mu\text{m}$ in the measurement area. A colour CCD camera with 1524×1012 pixels records the laser light scattered normal to the plane of the light sheet. Each pixel corresponds to $9\ \mu\text{m}$ in real space, providing a flow image over $14\ \text{mm} \times 9\ \text{mm}$ approximately.

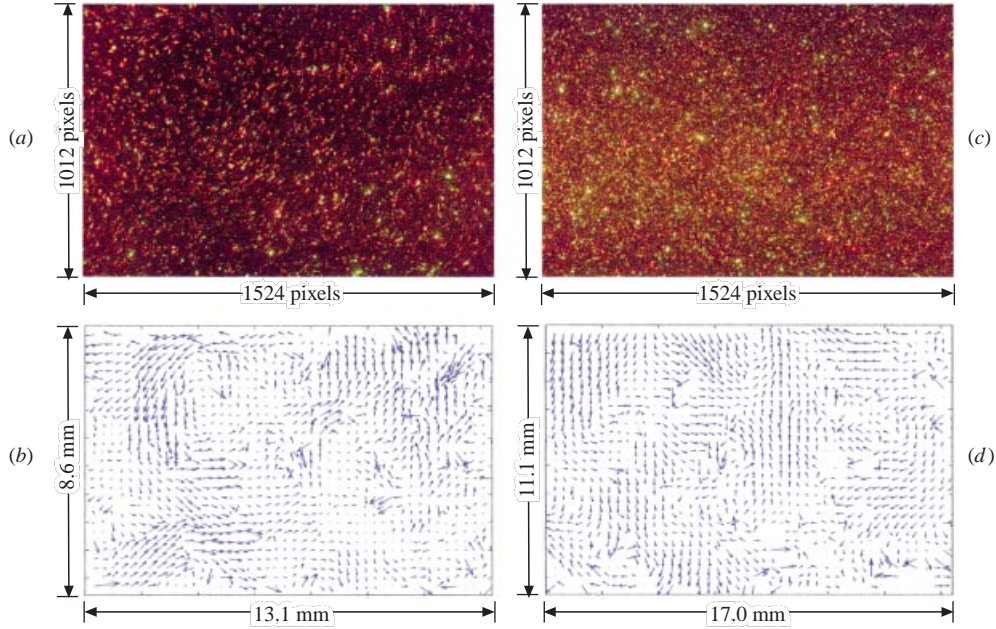


FIGURE 2. Typical PIV image (a) and the corresponding vector plot (b) taken in helium at a non-dimensional time $t_M = 40$ and a mesh Reynolds number $R_M = 3.3 \times 10^4$. (Both t_M and R_M are defined in §4.) (c, d). As (a, b) taken in nitrogen at $t_M = 850$ and $R_M = 9.1 \times 10^3$.

From the imaged particle positions, we obtain the velocity field by the cross-correlation technique. The technique calculates the correlation between the red and green intensity fields over an interrogation area and obtains an average velocity vector for that area. Here, the interrogation areas are 64 pixels on each side and have an overlap of 32 pixels. By repeating the analysis over all possible interrogation areas, we obtain 45 velocity vectors in the transverse direction y parallel to the grid, and 29 in the ‘streamwise’ direction x (vertically down). A typical PIV image and its corresponding vector plot are shown for helium measurements in figures 2(a) and 2(b), respectively. Nitrogen data in figures 2(c) and 2(d) are in general of better quality.

3. Data validation

The cross-correlation technique requires a particle population of the order 10 to be present in an interrogation area which, in general, should not be larger than the smallest scale in the flow. Since the particle loading has to be small, the spatial resolution of the PIV system is vitally dependent on the size of the particle tracers. The magnitude and direction of the average velocity over the interrogation area are given by the position of the peak in the correlation plane. If the interrogation area is larger than the smallest scales of motion the existence of velocity gradients within the area produces a spatial spread of the correlation peak when the gradients are weak and ‘false vectors’ when the gradients are large. These false vectors are produced by secondary peaks in the correlation function.

For the conditions chosen, the interrogation area varies between 50 and 15 Kolmogorov scales for helium and 15 and 3 Kolmogorov scales for nitrogen. This produces a signal with a non-trivial fraction of false vectors (of the order 5–30% for helium

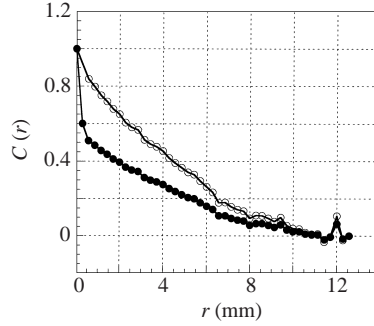


FIGURE 3. A typical cross-correlation function for helium data, before correction (●) and after correction (○) as described in the text. $R_M = 2 \times 10^5$, $t_M = 540$.

and 5–15% for nitrogen), and are the major source of noise. The influence of this noise has been mitigated by employing various available techniques as discussed in White (2001). A further source of noise due to the poor resolution of the small scales requires a different correction, as described below.

The noise and signal are uncorrelated, so a typical longitudinal correlation function $C(r) \equiv \langle (u(x)u(x+r))^2 \rangle / \langle (u(x)^2) \rangle$, where u and r are the velocity component and the separation distance in the direction x , contains at the origin a ‘delta function’ due to the noise (closed symbols in figure 3). We correct for this effect by using two methods. Both result in the effective removal of this spurious peak and the normalization of the remainder of the correlation function to restore unity value at the origin (open symbols in figure 3). In the first method, we determine the normalization factor, κ , by fitting the correlation function away from the origin to the classical Kolmogorov scaling relation (e.g. Frisch 1995) and extrapolating it to the origin. Neglecting small-scale intermittency effects, the fit is given by

$$\kappa - C(r) = \frac{C_k r^{2/3}}{2u'^2}. \quad (3.1)$$

Here, u' is the root-mean-square value of the fluctuating velocity u , the constant C_k (≈ 2 , see Sreenivasan 1995) subsumes the Kolmogorov constant and the energy dissipation; κ would, of course, be unity for noise-free data. The second method determines κ from the relation (Stolovitzky, Sreenivasan & Juneja 1993)

$$\kappa - C(r) = \frac{1}{2u'^2} \frac{\gamma r^2}{(1 + \xi r^2)^{0.65}}, \quad (3.2)$$

where γ and ξ can be treated as unknown parameters to be determined from a three-parameter least-square curve fit to the data. Expression (3.2) takes account of intermittency and fits the correlation function data in both inertial and dissipation ranges. The two sets of estimates of κ agree to within 10% for all measured times in the decay.

4. Principal results

We acquire data between $40t_M$ and $2000t_M$, where t_M is the mesh time $= tU/M$, M being the centre-to-centre spacing of the rods of the grid (‘mesh size’) and U the towing velocity. For each pull-through motion of the grid, only one image is acquired at a fixed time Δt after the grid has moved past the imaged area. Helium data are

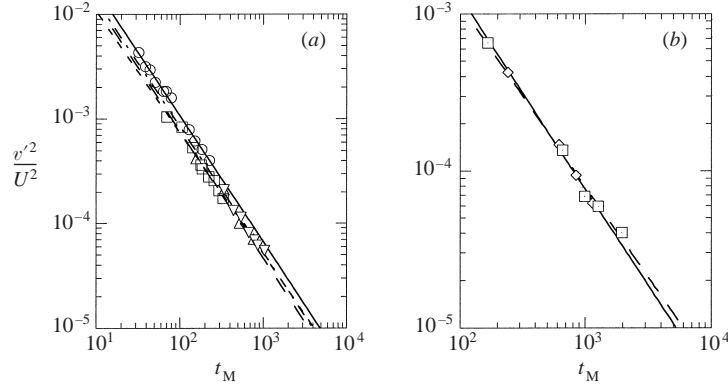


FIGURE 4. Temporal decay of the mean-squared-velocity fluctuation in the direction of motion of the grid at four Reynolds numbers for helium (*a*) and two mesh Reynolds numbers for nitrogen (*b*). The lines through the data are the least-square power-law fits. In (*a*) \circ , —, $R_M = 3.3 \times 10^4$; \square , —, $R_M = 6.6 \times 10^4$; \triangle , \cdots , $R_M = 1.32 \times 10^5$; ∇ , $-\cdot-\cdot-$, $R_M = 2.0 \times 10^5$. In (*b*) \diamond , —, $R_M = 9.1 \times 10^3$; \square , —, $R_M = 1.82 \times 10^4$. The Reynolds numbers remain large to the end of the range (so no ‘final period of decay’ is possible), and it is estimated that the boundary layer effects are negligible except perhaps for the last symbol for the nitrogen data.

acquired for six mesh Reynolds numbers $R_M \equiv UM/\nu$ of 3.3×10^4 , 5.0×10^4 , 6.6×10^4 , 1.3×10^5 , 2.0×10^5 , and 7.1×10^5 . Nitrogen data are acquired for two mesh Reynolds numbers, 9.1×10^3 and 1.8×10^4 . The Reynolds number is varied by changing the mesh size (as noted in §2.1) and the towing speed of the grid. For each R_M and each Δt we obtain an ensemble of images. For brevity, we present helium results for the grid of mesh size 3.33 mm, used to generate all but the smallest and the largest R_M .

For each image, statistical quantities such as correlations are ensemble averaged over columns for the streamwise velocity and rows for the transverse. The mean-square velocities in the streamwise and transverse directions differ by only about 5% over the measurement conditions, suggesting that turbulence is essentially isotropic on the large scale. (In contrast, most wind tunnel data possess higher anisotropy.) We present results only for the transverse component partly because the number of grid points in that direction is larger and so the statistics are better, and partly because the presence of a very small streamwise average velocity (of the order of $0.005U$ for $t_M > 100$) in each image complicates the process of ensemble averaging for u' .

Figure 4 shows the time decay of the mean-square turbulent transverse velocity normalized by U^2 . The data are fitted to the power law, $\alpha t_M^{-\beta}$. The values of α and β for the helium data, are, respectively, 0.28 and 1.21 for $R_M = 3.3 \times 10^4$, and 0.21 and 1.22 for $R_M = 6.6 \times 10^4$, 0.16 and 1.16 for $R_M = 1.32 \times 10^5$, and 0.22 and 1.21 for $R_M = 2.00 \times 10^5$. For the nitrogen data they are, respectively, 0.36 and 1.22 for $R_M = 9.1 \times 10^3$, and 0.23 and 1.15 for $R_M = 1.8 \times 10^4$. The statistical uncertainty in β is less than ± 0.1 . The differences among the three data sets are due more to differences in initial conditions. Because we have a sizeable range of decay times, no virtual origin has been used (see Mohamed & LaRue 1990 for a discussion of this point).

The exponent for the first few hundred mesh distances has been measured by Comte-Bellot & Corrsin (1966) to be about 1.2, with α values ranging from 0.02 to 0.1 depending on initial conditions (see, also, Sreenivasan *et al.* 1980). Since α is a measure of the initial turbulent energy, it is plausible that the higher α for the present measurements is due to the large initial accelerations of the grid. This view

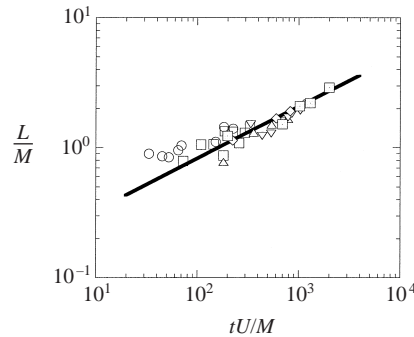


FIGURE 5. Temporal development of the integral length scale L for six mesh Reynolds numbers. \circ , $R_M = 3.3 \times 10^4$; \square , $R_M = 6.6 \times 10^4$; \triangle , $R_M = 1.32 \times 10^5$; ∇ , $R_M = 2.00 \times 10^5$; \diamond , $R_M = 9.1 \times 10^4$; \square , $R_M = 1.82 \times 10^4$. The solid line is the best fit for the wind tunnel data (Sreenivasan *et al.* 1980). When translated to the present case, that fit is $L/M = 0.13(tU/M)^{0.4}$.

seems consistent with the fact that active grids with dynamically accelerating and decelerating elements in them have larger values of α (Mydlarski & Warhaft 1996).

The ‘longitudinal’ integral length scale L is obtained (obviously, without Taylor’s hypothesis) by evaluating the area under the (normalized) correlation function of the transverse velocity component v at any point with v at another point separated by r in the transverse direction y . For separation distances r greater than about half the image size, the correlation function, generated by performing ensemble averages along rows in PIV images, does not converge well because of insufficient data. So, the measured correlation function is fitted to the inertial-range power-law for r smaller than half the image size and extrapolated to the full span of the measurement window before performing the integral. The results are shown in figure 5 and compared with earlier wind tunnel data (Sreenivasan *et al.* 1980) by converting space in those experiments to time in ours through the flow velocity. Except for small times, say $t_M < 50$, the agreement among the seven sets of data and with the previous best fit is within experimental uncertainty, which is in the range of 0.25–0.5 mm for L .

The Taylor microscale λ , defined through the relation $\varepsilon = 15v(v'^2/\lambda^2)$ where ε is the dissipation rate per unit mass, is obtained by two independent methods. In the first method, ε is obtained from the energy decay in figure 4, $\varepsilon = -(3/2)(dv'^2/dt)$, while in the second, it is obtained from Kolmogorov’s relation (see e.g. Frisch 1995) for second-order structure function S_2 , namely $S_2(r) = C_k(r\varepsilon)^{2/3}$, where $S_2(r) \equiv \langle (v(y+r) - v(y))^2 \rangle$ and every other quantity but ε is known. The second-order structure function is computed for each Δt and fitted to the 2/3-power in r . The agreement between the λ values calculated by two independent methods, shown in figure 6, is reassuring. The Taylor microscale Reynolds number $R_\lambda = v'\lambda/v$ can now be computed to be 130, 180, 195, 260, 310 and 575 for helium, and 80 and 120 for nitrogen.

The quantity $\varepsilon L/v'^3$ is a measure of the ratio of the time scale for the energy transfer to that of the energy-containing eddies, and is believed to be a constant of the order unity, independent of the Reynolds number for large enough Reynolds numbers (e.g. Frisch 1995). Various experimental data for grid turbulence, collected by Sreenivasan (1984), show that $\varepsilon L/v'^3$ asymptotes to a constant for $R_\lambda \geq 70$; see also Stalp (1998) for data in helium II. Direct numerical simulations of isotropic turbulence show a similar behaviour (Sreenivasan 1998). The present data are plotted in figure 7. The open symbols and \times use the measured value of L . The large scatter of 20–40% is due mostly to the uncertainty in L . This is clear because when L from the fit shown

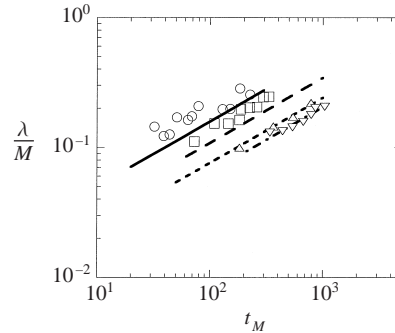


FIGURE 6. Temporal development of the Taylor microscale λ obtained by two different methods, for the four mesh Reynolds numbers in liquid helium; symbols as in figure 4(a). The lines indicate λ values obtained from the energy decay in figure 4. The symbols are λ values obtained from the second-order structure function. The agreement between the two results improves with increasing Reynolds number.

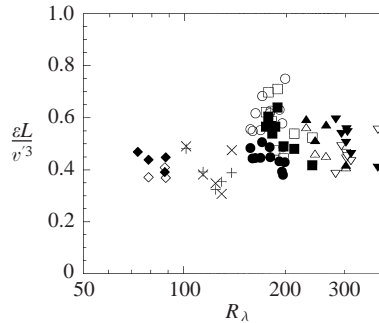


FIGURE 7. $\varepsilon L/v^3$ as a function of R_λ . Open symbols use the measured integral scale and filled symbols use the fit shown in figure 5. Symbols are: \circ, \bullet , $R_M = 3.3 \times 10^4$; \square, \blacksquare , $R_M = 6.6 \times 10^4$; $\triangle, \blacktriangle$: $R_M = 1.32 \times 10^5$; $\nabla, \blacktriangledown$, $R_M = 2.0 \times 10^5$; \diamond, \blacklozenge , $R_M = 9.1 \times 10^4$; \square, \boxplus , $R_M = 1.82 \times 10^4$.

in figure 5 is used instead, a significant reduction in scatter occurs (filled symbols and \boxplus). It appears that $\varepsilon L/v^3$ is indeed a constant in these measurements and has the average value of about 0.5. We have discussed elsewhere (Sreenivasan 1998, White 2001) that the asymptotic value of $\varepsilon L/v^3$ depends on initial conditions (or the nature of 'forcing').

5. Conclusions

The present work is part of a programme aimed at exploiting the merits of cryogenic helium for turbulence studies. Here, we have shown that detailed spatial measurements of turbulence can be made in cryogenic helium. With non-trivial modifications required in scaling up of the facility as well as optics, the Reynolds numbers can be exceeded by a factor 10 and the accuracy of the technique improved. This will undoubtedly enhance the ability to measure turbulence at very high Reynolds numbers in small apparatus, thereby making major advances possible in a single-investigator laboratory. It should also be stressed that the agreement of the helium data with those in other flows is a strong evidence that helium turbulence indeed obeys the Navier–Stokes equations (a question that has sometimes been raised in the past).

We thank J. J. Niemela, W. F. Vinen and R. J. Donnelly for their invaluable help in the design of the cryogenic apparatus, and for educating us on low temperature research. The work was supported by the US National Science Foundation, grant DMR-95-29609. Most of the equipment was purchased under the ONR DURIP grant subcontracted from Boston University.

REFERENCES

- BATCHELOR, G. K. & TOWNSEND, A. A. 1948 Decay of isotropic turbulence in the initial period. *Proc. R. Soc. Lond. A* **193**, 539–558.
- CASTAING, B., CHABAUD, B. & HEBRAL, B. 1996 Hot-wire anemometer operating at cryogenic temperatures. *Rev. Sci. Instrum.* **63**, 4167–4173.
- CHEN, S. Y., DOOLEN, G. D., KRAICHNAN, R. H. & SHE, Z. S. 1993 On statistical correlations between velocity increments and locally averaged dissipation in homogeneous turbulence. *Phys. Fluids A* **5**, 458–463.
- COMTE-BELLOT, G. & CORRSIN, S. 1966 Use of a contraction to improve isotropy of grid-generated turbulence. *J. Fluid Mech.* **25**, 657–682.
- DICKEY, T. & MELLOR, G. L. 1980 Decaying turbulence in neutral and stratified fluids. *J. Fluid Mech.* **99**, 13–30.
- DONNELLY, R.J. & SREENIVASAN, K.R. 1998 *Flow at Ultra-High Reynolds and Rayleigh Numbers*. Springer.
- FRISH, U. 1995 *Turbulence: The Legacy of A. N. Kolmogorov* Cambridge University Press.
- GAD-EL-HAK, M. & CORRSIN, S. 1974 Measurements of nearly isotropic turbulence behind a uniform jet grid. *J. Fluid Mech.* **62**, 115–143.
- JIMENEZ, J., WRAY, A. A., SAFFMAN, P. G. & ROGALLO, R. S. 1993 The structure of intense vorticity in isotropic turbulence. *J. Fluid Mech.* **255**, 65–90.
- MAXEY, M. R. & RILEY, J. J. 1983 Equation of motion for a small rigid sphere in a nonuniform flow. *Phys. Fluids* **26**, 883–889.
- MEI, R., ADRIAN, R. J. & HANRATTY, T. J. 1991 Particle dispersion in isotropic turbulence under Stokes drag and Basset force with gravitational settling. *J. Fluid Mech.* **225**, 481–495.
- MOHAMED, M. S. & LARUE, J. C. 1990 The decay power law in grid-generated turbulence. *J. Fluid Mech.* **219**, 195–214.
- MYDLARSKI, L. & WARHAFT, Z. 1996 On the onset of high-Reynolds-number grid-generated wind tunnel turbulence. *J. Fluid Mech.* **320**, 331–368.
- SREENIVASAN, K. R. 1984 On the scaling of the turbulence energy dissipation rate. *Phys. Fluids* **27**, 1048–1051.
- SREENIVASAN, K. R. 1995 On the universality of the Kolmogorov constant. *Phys. Fluids* **7**, 2778–2784.
- SREENIVASAN, K. R. 1998 An update on the energy dissipation rate in isotropic turbulence. *Phys. Fluids* **10**, 528–529.
- SREENIVASAN, K. R., TAVOULARIS, S., HENRY, R. & CORRSIN, S. 1980 Temperature-fluctuations and scales in grid-generated turbulence. *J. Fluid Mech.* **100**, 597–621.
- STALP, S. 1998 Decay of grid turbulence in superfluid turbulence. PhD thesis, University of Oregon.
- STALP, S., NIEMELA, J. J. & DONNELLY, R. J. 2000 Effective kinematic viscosity of turbulence in superfluid He-4. *Physica B* **284**, 75–76.
- STOLOVITZKY, G., SREENIVASAN, K. R. & JUNEJA, A. 1993 Scaling functions and scaling exponents in turbulence. *Phys. Rev. E* **48**, R3217–R3220.
- TABELING, P., ZOCCHI, G., BELIN, F., MAURER, J. & WILLAIME, H. 1996 Probability density functions, skewness, and flatness in large Reynolds number turbulence. *Phys. Rev. E* **53**, 1613–1621.
- VINCENT, A. & MENEGUZZI, M. 1994 The dynamics of vorticity tubes in homogeneous turbulence. *J. Fluid Mech.* **258**, 245–254.
- WHITE, C. M. 2001 High Reynolds number turbulence in small apparatus. PhD Thesis, Yale University.
- WU, X.-Z. 1991 Along the road to developed turbulence: Free thermal convection in low temperature helium gas. PhD Thesis, University of Chicago.